Nondestructive characterization of solar PV cells defects by means of electroluminescence, infrared thermography, I-V curves and visual tests: experimental study and comparison

Sara Gallardo-Saavedra [a *], Luis Hernández-Callejo [a], María del Carmen Alonso-García [b], José Domingo Santos [b], José Ignacio Morales-Aragonés [a], Víctor Alonso-Gómez [a], Ángel Moretón-Fernández [c], Miguel Ángel González-Rebollo [c] and Oscar Martínez-Sacristán [c].

[a] Universidad de Valladolid (UVa), School of Forestry, Agronomic and Bioenergy Industry Engineering (EIFAB), Department of Agricultural and Forestry Engineering, Campus Duques de Soria, 42004, Soria, Spain.

[b] Photovoltaic Solar Energy Unit (Energy Department, CIEMAT), Avda. Complutense 40, 28040 Madrid, Spain.

[c] Universidad de Valladolid (UVa), Department of Condensed Matter Physics, GdS Optronlab Group, Paseo de Belen 19, 47011, Valladolid, Spain.

*Corresponding author. E-mail addresses: sara.gallardo@uva.es (S. Gallardo-Saavedra).

Abstract

Photovoltaic (PV) modules are the core of every PV system, representing the power generation and their operation will affect the overall plant performance. It is one of the elements within a PV site with the higher failure appearance, being essential their proper operation to produce reliable, efficient and safety energy. Quantitative analysis and characterization of manufacturing, soldering and breaking PV defects is performed by a combination of electroluminescence (EL), infrared thermography (IRT), electrical current voltage (I-V) curves and visual inspection. Equivalent-circuit model characterization and microscope inspection are also performed as additional techniques when they contribute to the defects characterization. A 60-cells polycrystalline module has been ad hoc manufactured for this research, with different defective and non-defective cells. All cells are accessible from the backside of the module and the module includes similar kinds of defects in the same bypass string. This paper characterizes different defects of PV modules to control, mitigate or eliminate their influence and being able to do a quality assessment of a whole PV module, relating the individual cells performance with the combination of defective and non-defective cells within the module strings, with the objective of determining their interaction and mismatch effects, apart from their discrete performance.

Keywords

PV defects; PV characterization; Cold-spot; Manufacturing PV defects; Soldering PV defects; Breaking PV defects.

1. Introduction

The recent growth in renewable power capacity has been led by solar photovoltaics (PV), with 100 GW of new solar PV capacity installed in 2018 of the more than 180 GW of renewable power installed this year, reaching a total installed PV solar capacity of 505 GW [1,2]. Current research and development in PV systems is principally focused on higher efficiency and lower cost, improved designs of PV systems, as well as optimal operation and maintenance (O&M), which is the key to large scale applicability PV systems [3,4]. PV modules are the core of every PV system, representing the power generation and their operation will affect the overall plant performance. It is one of the elements within a PV site with the higher failure appearance, with a Mean Time Between Failures (MTBF) of 63.2 kW*year/failure [5], which means that each year there is an O&M alarm to repair a component within the PV generator (including the PV modules, junction boxes with the bypass diodes, structures, DC wiring, combiner boxes and electrical DC protections) each 63.2 kW installed in a PV site. According to Ref. [5], 8.5% of the failures within a PV site are due to the PV generator, which could be higher considering that the systems upstream inverter are not usually monitored, so these alarms are not automatically generated. Being able to detect, to identify and to quantify the severity of defects that appear within PV modules is essential to constitute a reliable, efficient and safety system, avoiding energy losses, mismatches and safety issues.

Defects at the PV solar cells level are really important, since these are the ones that make up the defects at the PV modules, being responsible for the reduction of efficiency, as well as their durability and reliability [6]. There has been extensive research on the types of failures and their finding [5,7–11], as it would be interesting to have them classified and even being able to estimate them. The failures in the plants are numerous and very heterogeneous, so their research is a challenge of interest to the scientific world [12–14]. Faults can appear in manufacturing, transportation, installation and operation [15]. The soldering of the wires to the solar cells results in generating significant thermomechanical stresses in different layers due to the diversity of thermal expansion of different components, which can lead to small cracks in the solar cells [16,17]. In ref. [18], four different groups of failures are defined, according to the type of PV technology, stablishing the common failures modes to all PV modules as delamination, back sheet adhesion loss, junction box failure and frame breakage, and the failures in silicon wafer-based PV modules as EVA discoloration, cell cracks, snail tracks, burn marks, Potential Induced Degradation (PID), disconnected cell, string interconnect ribbons and defective bypass diode.

Different techniques have been historically used to identify faulty modules and cells. The quickest method to find failures in a PV module is the visual inspection [18], but it only reveals some of the failures, as bubbles, delamination, yellowing, browning, broken cells, oxidized or burned cells, corrosion or exposed electrical parts. Additionally to a simple visual inspection, it can also be useful using the microscope, which offers enhanced images of defects that apparently are invisible. A comprehensive knowledge of the properties of defects requires electrical characterization techniques providing some information about the defect concentration, spatial distribution or physical origin [19]. The current-voltage (I-V) characterization provides the most information of the performance of any type of PV device [20], and its main parameters, but it cannot be performed in common operation neither locate the exact position of defects. An accurate I-V curve interpretation gives relevant information about the module failures, revealing degradation, mismatched modules, cracked cells, improper

resistance, shadings or bypass diodes malfunction [21]. Infrared thermography (IRT) can be carried out in both indoor (dark) and outdoor (illuminated) conditions and it is a technique that detects heat distribution in an evaluated area. This technique has the great advantage that it is applied with the PV plant in operation, measuring the characteristics of radiative heat in order to set areas or points with higher or lower heat emissivity, areas that could indicate the presence of a fault. The requirement of minimal instruments and non-contact application make IRT very attractive. Completing the inspection techniques, EL imaging is another established non-destructive technology for failure analysis of PV modules in which defective cells appear darker, because disconnected parts do not irradiate [22]. It can be used in the manufacturing process, shipped to a lab after unmounting the modules from the site or on the field, with a structure or specific tripod or also by means of EL cameras mounted on UAVs. In this case, by means of this non-invasive technique, the radiative recombination of charge carriers causes light emission in the solar cells, which is captured by an EL camera and the emission intensity serves as an indicator of the healthiness of the solar cell [23–25]. The high spatial image resolution enables the detection of micro cracks due to the silicon Charge-Coupled Device (CCD) sensor high resolutions. According to [6], IRT and EL imaging are efficient and powerful methods for characterization of PV panels. . As it has been seen, each of these techniques has some advantages and disadvantages, and based on them, PV plant operators usually apply only one of these techniques within the O&M activities.

Authors in [22] recommend to use the most appropriate method for defect detection considering the structure of site, parameters to be measured and other factors, as the predominant defect types. In this context, the aim of this research is not proposing any improved inspection technique, as standard tests have been applied. Previous authors mainly work with the different inspection techniques separately. However, it is important to know the information provided by each of these inspection techniques considering the defect type, with the objective of not missing any information during the inspection. As a new approach, it is proposed the joint study of three specific PV defects with different techniques, which allow analyzing their complementarity. Therefore, the main goal of this paper is to characterize three different types of defects in PV cells, manufacturing, soldering and breaking PV defects, using RGB and microscope images, I-V curves, IRT indoor and outdoor and EL techniques. This research helps to understand the knowledge provided by each technique from these defects, with the final objective of properly control, mitigate or eliminate their influence and being able to do a quality assessment of these kind of defects within a module. In relation with the available literature, it has been notice that a clear understanding of the relationship between the underlying material characteristics and device performance is still lacking. This paper also relates the individual cells performance with the combination of defective and non-defective cells within the module strings, with the objective of determining their interaction and mismatch effects, apart from their discrete performance.

2. Method

2.1. Tested module

For the research development, a singular polycrystalline module composed of different defective and non-defective cells has been ad hoc designed. The module has been manufactured

with cells of three buses. The front and back views of the module are presented in Fig. 1 a) and b), respectively. In order to be able to analyze the module in detail, all cells are accessible from the backside of the module. For the cell labelling, it has been used numbers from 1 to 10 to identify the cell row and letters from A to F to identify the column, as it can be seen in Fig. 1 c). In the three images, Fig. 1, the module junction box is placed in the top part of the image. It is not represented in Fig. 1 c) to avoid covering cells.

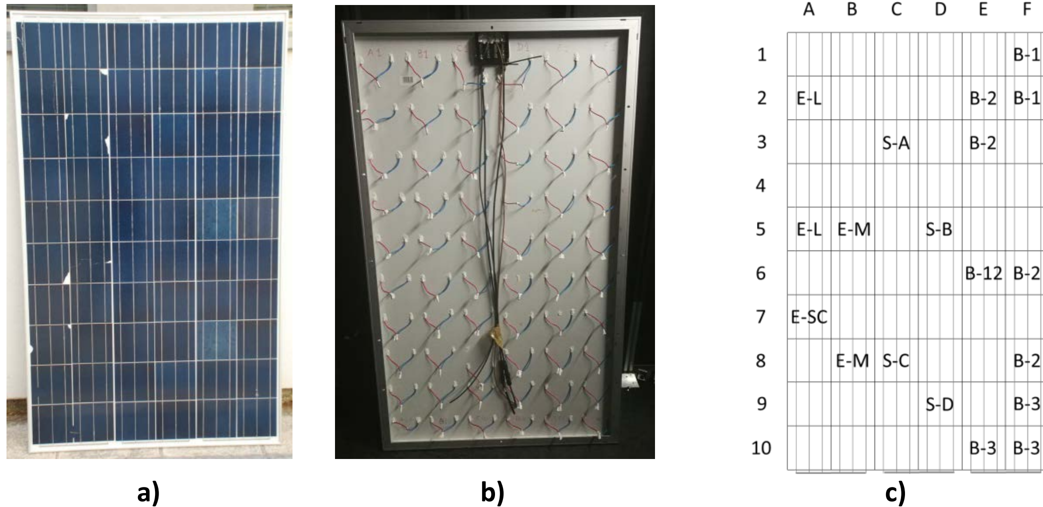

Fig. 1. a) Front view of the tested module. b) Back view of the tested module. c) Defective cells distribution showed in the back view of the tested module.

The module has been designed including similar kinds of defects in the same string. In this way, the string corresponding to columns A and B (string AB) contains manufacturing defects, the string CD contains soldering faults while the string EF contains breaking deficiencies. The defects of the three module strings are summarized in Table 1. The low efficiency defects (defect E-L, cells A2 and A5) are due to manufacturing problems, but they do not correspond with breaking or short-circuited cells. Short-circuit cell (defect E-SC, cell A7) has been generated by extending the cell connection tabs beyond the ordinary placement, short-circuiting the cell. In order to simulate the bad soldering defects, buses from the back of some cells have been left without soldering, either one bus (defect S-A, cell C3) or two buses (defect S-B, cell D5). Three buses have not been left without soldering in any case as it would had meant that this cell would not be series connected to the rest. The cell with only 1cm welded (defect S-C, cell C8) simulates a bad soldering, in which only 1 cm of the bus is welded instead of the typical 15 cm welded. When a piece of broken cell is placed on top of another cell (defect B-3, cells E10, F9 and F10), what it really generates is a partial shading. It could simulate an important permanent bird crap. These types of defects are analyzed as they ordinarily appear in commercial modules in operation, either in manufacturing, transport or operation. However, commercial modules are not accessible at the cell level. That is why an ad hoc module has been manufactured for the defects characterization.

Table 1.

Cells defects types and codes per string.

	Defect code	**Defect type**	**Cell affected**
String AB – Manufacturing defects (E)	E-L	Low efficiency cell (9%)	A2, A5
	E-M	Medium efficiency cell (16.4%)	B5, B8
	E-SC	Short-circuited cell	A7
String CD –	S-A	One bus without soldering	C3

Soldering defects (S)	S-B	Two buses without soldering	D5
	S-C	Only 1cm of each bus welded	C8
	S-D	All tabs loose (without soldering)	D9
String EF – Breaking defects (B)	B-1	Split cell (without cell area decrease)	F1, F2
	B-2	Cracked cell (with cell area decrease)	E2, E3, F6, F8
	B-12	Defects B-1 and B-2 in the same cell	E6
	B-3	Piece of other broken cell over the cell surface	E10, F9, F10

The nominal characteristics of a standard module of this type (without the defective cells introduced in it for this research) are: nominal power (P) 250 W, efficiency 15.35%, maximum power point current (Impp) 8.45 A, maximum power point voltage (Vmpp) 29.53 V, short circuit current (Isc) 8.91 A and open circuit voltage (Voc) 37.6 V. Having 60 cells in series, the nominal values of a healthy cell have being considered: nominal power 4.17 W, Impp 8.45 A, Vmpp 0.49 V, Isc 8.91 A and Voc 0.63 V. This information has been used to analyze the effect of defects comparing with the nominal values.

2.2. Facilities,experimental techniques and software

The experimental techniques used in the characterization and the facilities in which the measurements have been performed are described in this section.

Firstly, the indoor measurements have been performed in the commercial system Pasan SunSim 3CM, that consists of a light pulse solar simulator class AAA according to IEC 60904-9 standard, which can perform I-V curve measurements at Standard Test conditions and at different irradiances by using irradiance masks. The system has an expanded combined uncertainty UC 95% (k=2) de 2,26% for Isc, 0.52% for Voc, 0.20% for FF and 2.33 % for Pmax (calibrated under PERFORMANCE project[1])..

The I-V curves were performed at two different irradiance levels, 1,000 W/m^2 and 100 W/m^2, with temperature controlled conditions of 25±0.5ºC. This temperature has been controlled with an air fan, and measured in two points of the module using a digital Fluke 54 II B thermometer with two thermocouples type T. The second irradiation level has been chosen to characterize the defects behavior in low irradiation conditions. The module is hanging in front of the solar simulator, in a structure in one of the walls of the solar chamber, as it can be seen in Fig. 2. The irradiance produced by the simulator falls upon the module surface perpendicularly.

With the objective of better characterizing the defects behavior, EL tests to individual cells have been performed to identify the light emission caused by radiative recombination of carriers in each case. During this EL test, the temperature of the different cells has been measured with thermography. The EL and indoor IRT tests simultaneously to the EL have also been taken in this chamber. In this case, the module is fed with a Delta power supply SM 70-22. A Fluke 189 multimiter connected to module terminals allow to register the exact module voltage. EL and IR images are captured with a PCO 1300 and a FLIR SC 640 camera, respectively. EL tests to

[1] PERFORMANCE. A science base on photovoltaic performance for increased market transparency and customer confidence. Project co-funded by the European Comission within the 6th Framewprk programme.

individual defective cells have been performed with an injected current of 8.9A, a focal distance of 4 cm and exposure time 40s. EL tests to the whole module have been performed at two injected current levels, 8.9A and 0.89A, with a focal distance of 4 cm and exposure time 50s and 15min, respectively. Flir SC 640 camera has an accuracy of ±2.0ºC or ±2% of the measurement and a thermal sensitivity of 0.06ºC. This image acquisition is presented in Fig. 2.

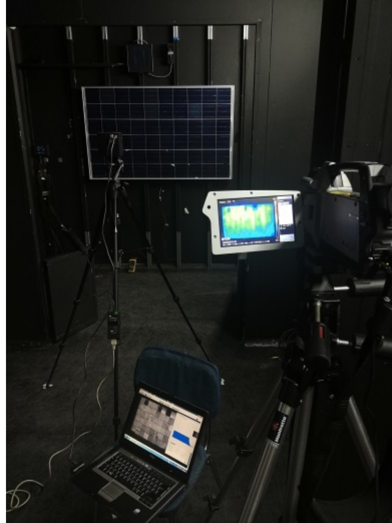

Fig. 2. Set up of the EL and IRT cameras for the indoor tests at the Photovoltaic Solar Energy Unit of the CIEMAT, in Madrid.

RGB images of the module have been taken with a Nikon D80 camera and images in detail of defects in the PV laboratory at the CIEMAT in Madrid with a Nikon SMZ 800 microscope. Finally, IRT has also been performed outdoor using the same IR camera, as presented in Fig. 3. To perform these images, the module has been biased with the systems used to perform outdoor I-V curve measurements, which consists of a DC power supply NLB 1400-125 connected to an Agilent 34980A measurements unit. A Kipp and Zonnen piranometer CM6B is used to measured irradiance. Additionally, a Fluke 189 multimeter is connected to module terminals to know the module voltage at their entrance. The temperature in the module cells has been measured with the same digital thermometer used indoors, and the resultant measurements have been used to calculate the emissivity and the reflected temperature values. These images have been taken in the lower current step of the I-V curve at 7.3A-24V and in the middle current step of the I-V curve at 7.8A-15V at 933W/m^2. Important aspects have been taken into account in the measurements, in order to make them valid. Firstly, it has been assured that measurements are done under steady state conditions of the PV module, on a sunny, clear, cloudless day, with at least 600 W/m^2 irradiation at the module array, according to standard [26]. It has been chosen a day in which the ambient temperature as well as the wind speed are low, with the aim of no influencing the hotspot or the module temperature, especially in the corner where the cooling effect is most important. The angle of view has been set as close as possible to 90° (not less than 60° to the module glass plane) [27].

Fig. 3. Outdoor IRT testing bench at the Photovoltaic Solar Energy Unit of the CIEMAT, in Madrid.

For the images and data processing, different software programs have been used. The main parameters of the single-diode model of a solar cell equivalent circuit have been calculated in the 2/3 Diode Fit software [28].For the image processing, apart from the own software of each equipment, it has been used ImageJ software [29] to obtain additional information from EL images, as an individual histogram of the light emission in each of the defective cells.

3. Results and discussion

This section summarizes the main results and contributions obtained in the research. It has been structured according to the different PV defects studied: manufacturing, soldering and breaking cell defects, to conclude with different defects combination and their correlation.

3.1. Manufacturing defects

Three different kinds of manufacturing defects have been studied, as detailed in Table 1: low efficiency (E-L), medium efficiency (E-M) and short circuited (E-SC) cells.

3.1.1. I-V characterization

All cells from the string have been electrically characterized by their I-V curves at 1,000W/m^2 and 100W/m^2. The electrical characteristic curves of the manufacturing defective cells at these irradiance levels are presented in Fig. 4 and Fig. 5, respectively, and the statistical values of the main parameters of the I-V curve of all the cells of this string at 1,000 W/m^2 are presented in Table 2. It can be seen that the maximum coefficients of variation, calculated as the standard deviation divided by the average value, appears in the Impp (13.59%) and in the power (16.57%). Large variations in the Impp values are responsible of important variations in the power generated by the string. This fact will be further analyzed in section 3.4. Defects combination /mix.

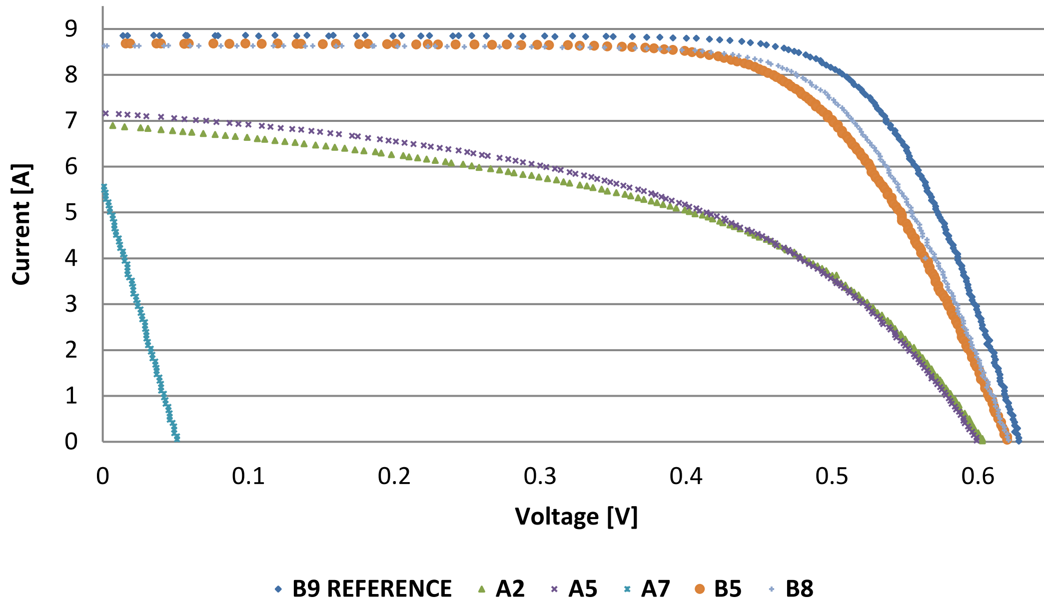

Fig. 4. I-V Curves of the manufacturing defective cells of the first string (string AB) at 1,000W/m^2, using B9 as the healthy reference cell of the string for comparison.

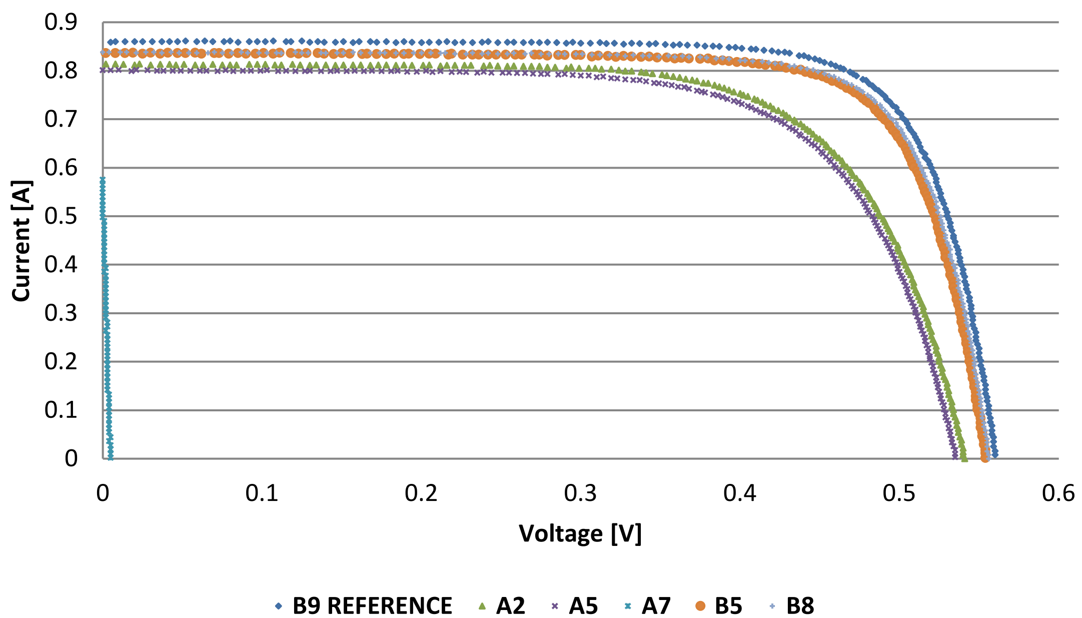

Fig. 5. I-V Curves of the manufacturing defective cells of the first string (string AB) at 100W/m^2, using B9 as the healthy reference cell of the string for comparison.

Table 2.
Statistical values of the main I-V curve parameters of the 19 cells of the manufacturing defects string inspected individually at an irradiation level of 1,000W/m^2. Short-circuited cell A7 has not been taken into account in the calculations so as not to misrepresent them.

Statistical values		P [W]	Impp [A]	Vmpp [V]	Isc [A]	Voc [V]
String AB	Mean	7.91	0.48	3.82	8.72	0.63
	Min	4.87	0.42	2.04	6.95	0.60
	Max	8.48	0.50	4.18	9.12	0.64

	Standard deviation	1.07	0.02	0.63	0.59	0.01
	Coefficient of variation	13.59%	4.86%	16.57%	6.79%	1.48%

The most widely used approaches for the electrical characterization of PV solar cells and modules are based on the real single-diode model of a solar cell equivalent circuit, which is based on the use of the equivalent circuit of a photodiode [30]. The main parameters of the defective cells have been calculated using this model in the 2/3 Diode Fit software [28] and they are presented in Table 3.

Table 3.
Main parameters of the defective cells of string AB using the single diode model at 2/3 Diode Fit [28] with the experimental data at 1,000W/m^2.

	Cell	A2	A5	B5	B8	B9 Reference
1-DIODE MODEL	J photo [mA/cm²]	29.89	31.02	35.70	35.49	36.41
	J 01 [A/cm²]	1.012E-09	6.05E-10	1.02E-09	1.09E-10	1.07E-10
	n1	1.46	1.40	1.40	1.24	1.25
	Rsh [Ohm*cm²]	112.75	115.36	4217.90	4977.90	11486.00
	Rs [Ohm*cm²]	7.91	8.06	2.14	1.88	1.42

As it can be seen from Fig. 4 and Fig. 5, manufacturing defects are much more evident at higher irradiance levels, having a greater impact. Their Fill Factor (FF) is reduced at higher irradiance levels and therefore their maximum power output. The low efficiency cells (A2 and A5) and the medium efficiency cells (B5 and B8) have a mean FF of 48.19% and 69.54%, respectively, at 1,000 W/m^2, versus 73.36% of the reference cell of the string at the same irradiance level. Typical FF values of polycrystalline silicon cells at Standard Testing Conditions (STC), that is T=298.15 K, W=1000 W/m^2 and AM1.5 G spectrum, are 75% to 80% [18]. On the other hand, their FF at low irradiance level (100 W/m^2) are 68.97%. 77.31% and 77.52%, respectively.

The medium efficiency defects present high values of series resistance (Rs) which can be seen in Fig. 4 as an increment in the curve slope at Voc and reduced FF. They also present low values of shunt resistance (Rsh), although not low enough to have a significant affection, as seen in the curve slope at Isc in Fig. 4. These facts are also appreciable in the modelled values in Table 3, in which Rs increases from 1.42 Ω/cm^2 in the reference cell B9 to 1.88 and 2.14 kΩ/cm^2 in B5 and B8, respectively, and Rsh decreases from 11.48 kΩ/cm^2 in the reference cell B9 to 4.21 and 4.97 kΩ/cm^2 in B5 and B8, respectively, using the single-diode model.

Otherwise, low efficiency cells have lower Rsh, which can be responsible of the decrement of Voc and the slope increment at Isc and higher Rs values, which additionally reduces the FF, as it increases the slope at Voc. Within the limitations of making a mathematical adjustment of these defective cells, which I-V curve is significantly different from the nominal one, they have also been modelled and their main parameters are in Table 3. At STC conditions it has been measured that the low efficiency defects can lead to an output power of 2.05 W, which compared with the reference cell of the string B9 that has an output of 4.08 W supposes a 49.76% of power loss. Within the limitations of modelling these curves, it is clearly observable uncommon ideality factor values n2 in cells A2 and A5.

3.1.2. EL and indoor IRT characterization

EL images of defective cells are showed in Fig. 6 and their indoor IRT in Fig. 7. IRT images have been taken with FLIR SC 640 IR camera. Their maximum and minimum temperatures in these conditions are (Fig. 7): a) T_{max}=38.8°C and T_{min}=29.1°C. b) T_{max}=40.6°C and T_{min}=30.8°C and c) T_{max}=33.0°C and T_{min}=27.6°C. Cells A2 and A5, which correspond with low efficiency cells, experiment a local overheating in the emitting area as it can be seen in the IR images presented in Fig. 7, a) and b), respectively. The short-circuited cell, A7, does not emit any light during EL as it can be seen in Fig. 6 c) and its whole area is seen colder in thermography, as seen in Fig. 7 c). Traditionally, when a cell or group of cells operates at abnormal temperature in a PV system it has been labelled as *hot spot* and this situation has been said to exist when a solar cell within a module generates less current than the string current of the module or of the PV generator [31]. This occurs when the cell is completely or partially shaded, damaged, or when cells are electrically mismatched. The shaded cell becomes reverse biased and dissipates power in the form of heat, which can be detected with IRT. Here, authors propose a new term, *cold spot*, defined as cell or group of cells at abnormal low temperature in a PV system. This effect is evident in the non-emitting areas during an EL test, in which these areas remain colder, as shown in Fig. 7 c). During outdoor operation, the three defective cells in Fig. 7 get hotter than the rest of cells, revealing as hot spots in outdoor IRT. This fact will be further analyzed in section 3.4.

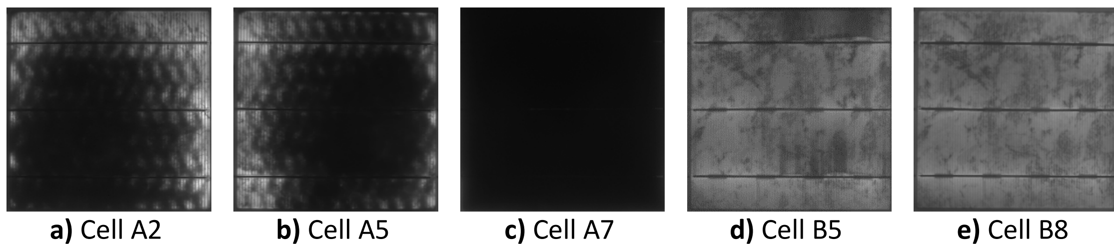

a) Cell A2 **b)** Cell A5 **c)** Cell A7 **d)** Cell B5 **e)** Cell B8

Fig. 6. EL images of the manufacturing defective cells of the first string (string AB) with an injected current of 8.9A. Images taken with PCO 1300 camera, with a focal distance of 4 cm and exposure time 40s.

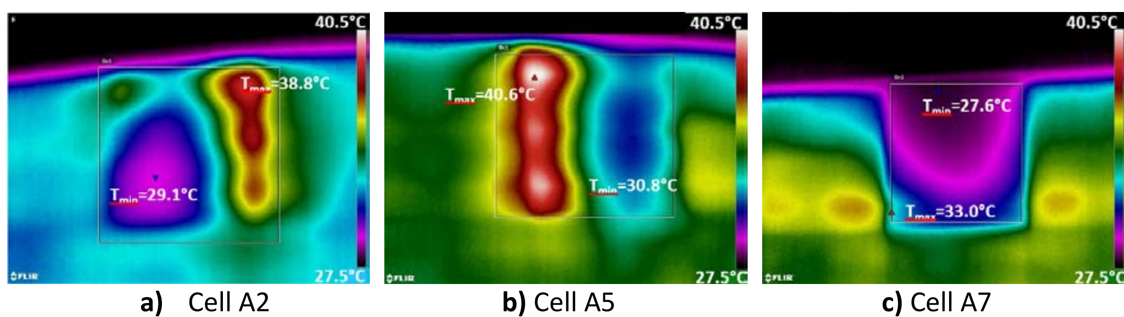

a) Cell A2 **b)** Cell A5 **c)** Cell A7

Fig. 7. Indoor IRT images of the low efficiency (a and b) and the short-circuited (c) defective cells of the first string (string AB) during EL tests, injecting current of 8.9A.

These low efficiency defects can be due to manufacturing imperfections. In Fig. 6 a) and b) it can be seen as a tire imprint in the cell EL images, which can be due to temperature inhomogeneity of the transport belt during the firing process of the cell producing [18]. Additionally, there is a central part in the cell that does not emit in these cells, which can be due to temperature inhomogeneity during firing process of the cell manufacturing that leads to center edge gradient

of contact resistance of the cell finger metallization [18]. Each of these two defects are classified separately as a failure that has no effect on safety with a power low below detection limit of 3% by the International Energy Agency (IEA) [18]. However, it has been seen that in this case there is a 49.76% of power loss.

It has been observed a tendency to decrease the light emission during EL tests with the efficiency drop. An individual histogram of the luminescence intensity of each defective cells has been obtained. The mean value of the resulting histogram is presented in Fig. 8 versus their power and FF. Cells A2 and A5 have the lowest power, FF and light emission levels while the reference cell B9 has the highest values.

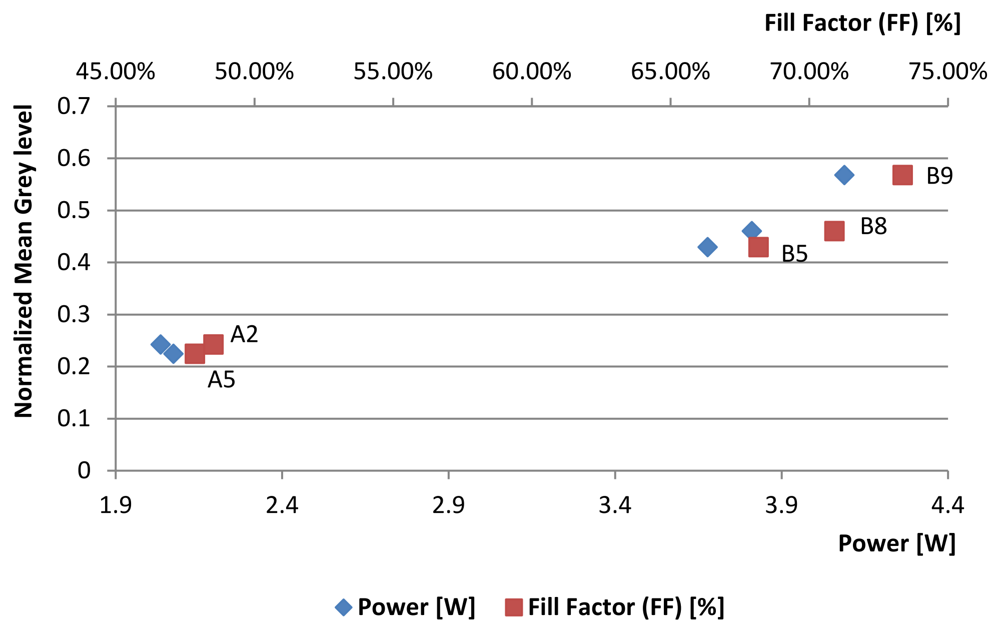

Fig. 8. Normalized Mean Grey level of the manufacturing defective cells of EL images captured with a PCO 1300 camera of 12 bits.

3.2. Soldering defects

3.2.1. I-V characterization

The electrical characteristic curves of the defective cells in the module string with soldering faults at 1,000 and 100 W/m^2 are presented in Fig. 9 and Fig. 10, respectively, and the statistical values of the main parameters of the I-V curve of the 20 cells of this string at 1,000 W/m2 are presented in Table 4. It can be seen that these cells present smaller parameter deviations than the previous defects, appearing the maximum coefficient of variation in the power (3.69%).

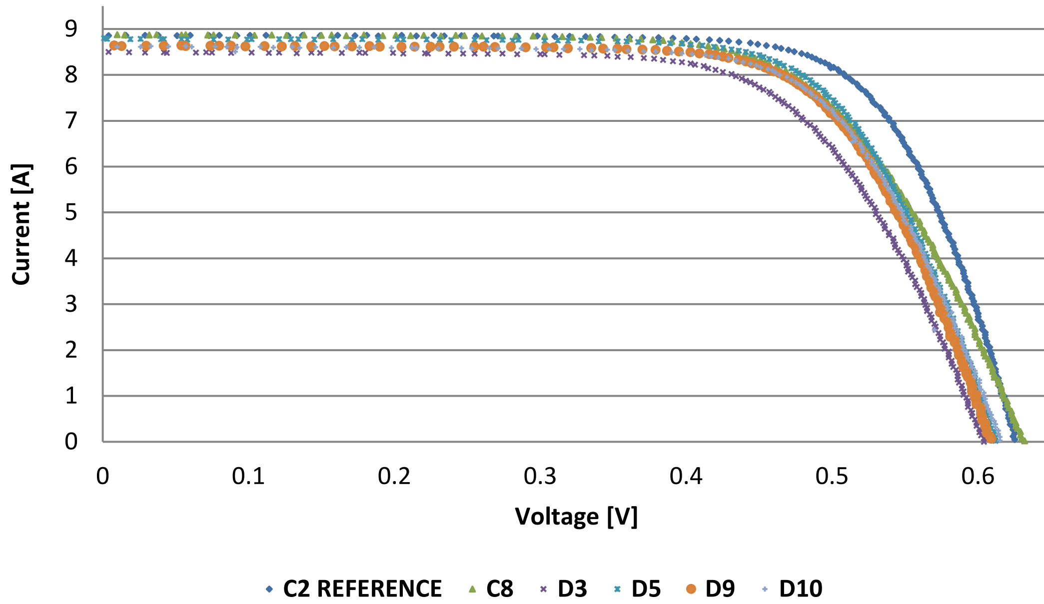

Fig. 9. I-V Curves of the soldering defective cells of the second string (string CD) at 1,000W/m^2, using C2 as the healthy reference cell of the string for comparison.

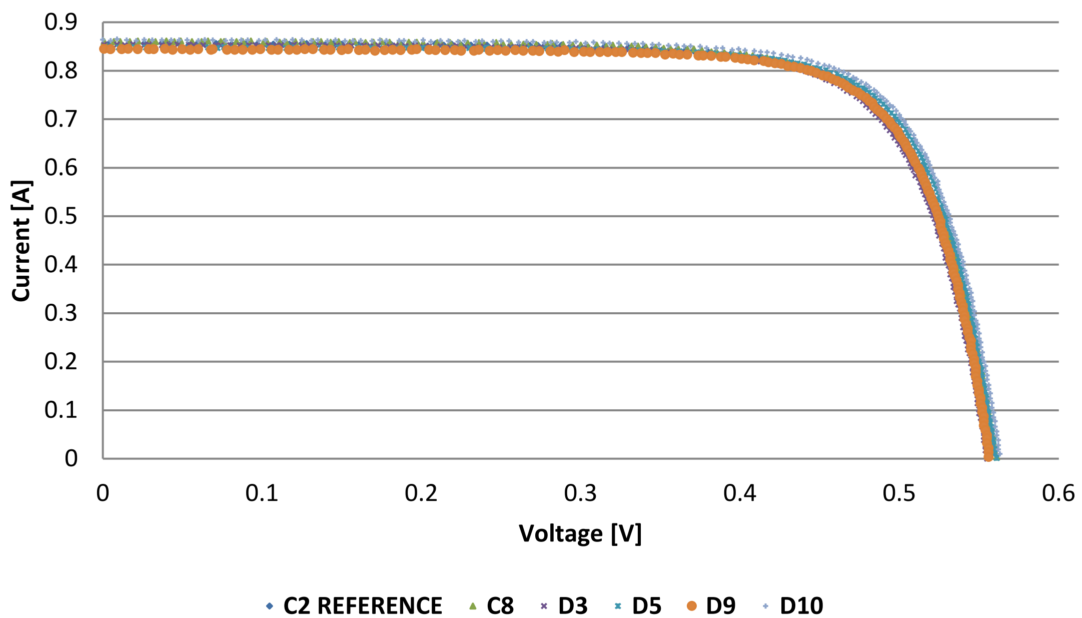

Fig. 10. I-V Curves of the soldering defective cells of the second string (string CD) at 100W/m^2, using C2 as the healthy reference cell of the string for comparison.

Table 4.
Statistical values of the main I-V curve parameters of the 20 cells of the soldering defects string inspected individually at an irradiation level of 1,000W/m^2.

Statistical values		P [W]	Impp [A]	Vmpp [V]	Isc [A]	Voc [V]
String CD	Mean	8.10	0.48	3.91	8.80	0.62
	Min	7.63	0.46	3.49	8.50	0.60
	Max	8.30	0.50	4.09	8.99	0.63
	Standard deviation	0.14	0.01	0.14	0.12	0.01

	Coefficient of variation	1.68%	2.51%	3.69%	1.31%	1.39%

The cell with only one centimeter welded (defect S-C. cell C8) simulates a bad soldering in which only one centimeter of the three buses is welded instead of the typical fifteen centimeters. In this case, all the current has to pass through a reduced surface, increasing the Rs of the cell (and of the module. consequently). This fact can be seen in Fig. 9 C8 cell I-V curve, in which the curve is strongly affected by the sRs near the Voc. Its Rs value could be estimated calculating the slope of the I-V curve at the Voc. The Voc is not affected by this Rs since the overall current flowing through the solar cell and through the resistance at this operation point is zero. The main impact of Rs is to reduce is nominal FF, although excessively high values may also reduce the short-circuit current [32].

The experimental FF values for C8 at 1,000 and 100 W/m^2 are 67.5% and 74.7%, respectively, versus 73.75% and 75.79% of the reference cell C2 at the same irradiance levels. As it can be seen, the current level has great impact on the losses due to Rs, having higher loses at higher current levels. The power loss in defective cells C3, D5, C8 and D9, described in Table 1, at STC conditions (Fig. 9) with respect the reference cell are 1.36%. 6.06%. 7.43% and 8.90%, respectively. However, at 100 W/m^2 (Fig. 10), this loss is just 0.28% in C8 and 0.83% in D9, while the fall in the rest of cells is negligible. It can be then concluded that the power loss at STC conditions when there is a bus not welded (with two buses collecting the electricity. as in C3) has just a 1.36% loses, which is less than the manufacturer tolerance of 2%. When there are two buses not welded (with just one bus out of three collecting the electricity, as in D5) it increases to 6.06%. However, there are more loses when there is a l, as the Rs is considerably increased, achieving the power loss 7.43% in C8. Additionally, it can be seen how having all tabs loose may not interrupt the current in a new manufactured module, as in cell D9 in the module used in this research, in which the power loss is 8.90% in spite of not having any tab welded. In this case, they can do electrical contact despite not being welded, and its influence is not disastrous. This fact could be altered after some years of operation of the module in which the encapsulation is exposed to thermal cycles (which can move from negative degrees at night to more than 40-50°C during the midday) and can begin to lose its compressive properties losing contact.

3.2.2. EL and indoor IRT characterization

The EL images of the faulty cells with an injected current of 8.9A are shown in Fig. 11. Soldering defects are not visible in EL. It could be because they are made on the backside of the module. An additional analysis has been performed to check if these defects are visible with IRT performed from the backside of the module in short circuit current injection conditions. The IRT image of the backside of the whole module can be seen in Fig. 12 a). Images taken with FLIR SC 640 IR camera. The maximum and minimum temperatures in C8 cell in these conditions are: Tmax=38.2°C and Tmin=29.6°C. In these conditions, it is seen in Fig. 12 a) that the only defect which certainly experiment an overheating is cell C8, corresponding the heating area with the centimeter of the three buses welded. This is clearly seen in Fig. 12 b), in which an IRT of the backside of cell C8 is presented. Therefore, defects with one or more buses not welded in the backside of the cell (cell C3 and D5) are apparently neither detectable using indoor IRT. It could be due to the metal sheet that covers the complete cell backside, which uniformly distributes the current that can be collected by the properly welded buses and the heat. Hence, hot spots

appear to be just detectable when there is a local soldering defect in just a part of the bus, as in this case the defect considerably increases the Rs, as it has been previously seen.

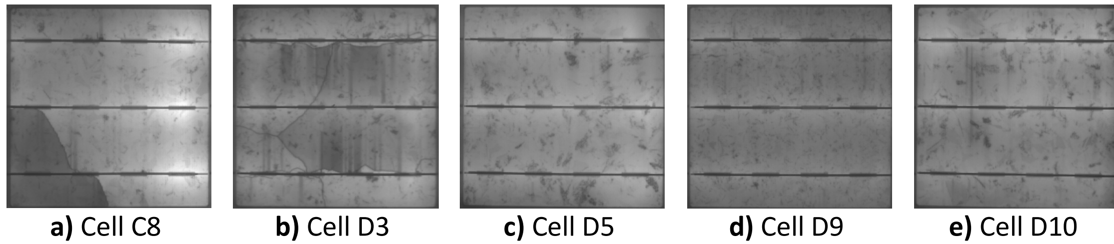

a) Cell C8 **b)** Cell D3 **c)** Cell D5 **d)** Cell D9 **e)** Cell D10

Fig. 11. EL images of the soldering defective cells of the second string (string CD) with an injected current of 8.9A. Images taken with PCO 1300 camera, with a focal distance of 4 cm and exposure time 40s.

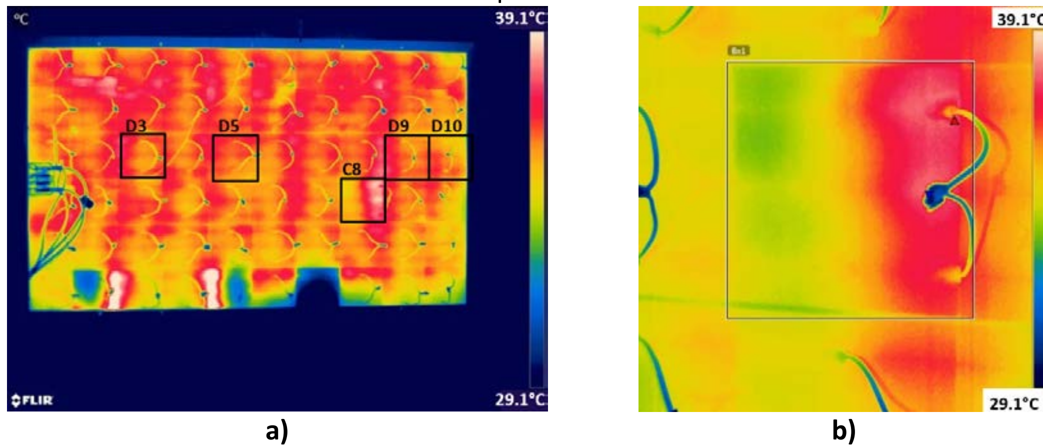

a) **b)**

Fig. 12. Indoor IRT images of the backside of the module (a) and of the C8 cell (b) during EL tests, injecting current of 8.9A.

The greatest danger of bad welds are usually the electric arcs, since that bad contact causes the tab to warm up and it can come out to disconnect it. At that moment you have a relevant tension difference between two points very close and micro arcs can be generated. That ends up burning the back sheet behind, or if they are generated in broken cells, the edges of the cell are usually burned and also depending on the composition of the paste together with the permeability of the back sheet, the humidity causes the fingers to blacken, being easily identifiable the cell breakages, which is commonly known as snail trails.

3.3. Broken cells defects

3.3.1. I-V characterization

The electrical characteristic curves of the defective cells in the module string with breaking faults at 1,000 and 100 W/m^2 are presented in Fig. 13 and Fig. 14, respectively, and the statistical values of the main parameters of the I-V curve of the 20 cells of this string at 1,000 W/m2 are presented in Table 5. It can be seen that the maximum coefficients of variation appears in the Impp (11.62%) and in the power (16.11%), similar to the manufacturing defective cells variations and higher than in the soldering defects string.

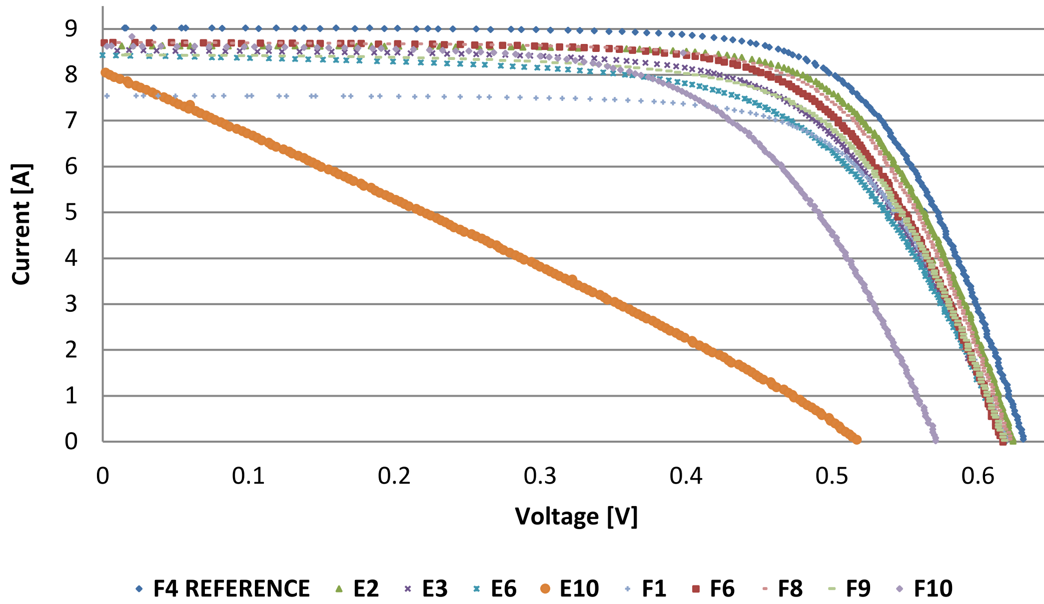

Fig. 13. I-V Curves of the broken defective cells of the third string (string EF) at 1,000W/m^2, using F4 as the healthy reference cell of the string for comparison.

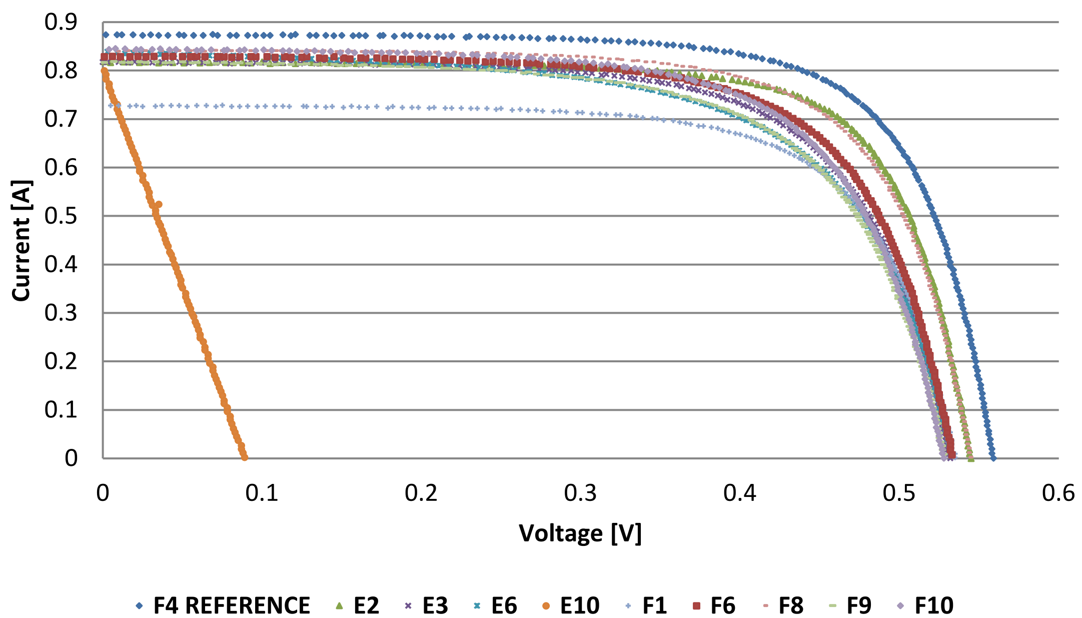

Fig. 14. I-V Curves of the broken defective cells of the third string (string EF) at 100W/m^2, using F4 as the healthy reference cell of the string for comparison.

Table 5.
Statistical values of the main I-V curve parameters of the 20 cells of the breaking defects string inspected individually at an irradiation level of 1,000W/m^2.

Statistical values		P [W]	Impp [A]	Vmpp [V]	Isc [A]	Voc [V]
String EF	Mean	7.62	0.46	3.56	8.68	0.62
	Min	4.17	0.33	1.36	7.55	0.56
	Max	8.26	0.49	4.03	9.03	0.63

	Standard deviation	0.89	0.04	0.57	0.35	0.02
	Coefficient of variation	11.62%	7.90%	16.11%	4.03%	2.95%

The study of cracks in cells is similar to the shading case. In general, the shadow may be fully or partially according to the percentage of area that shades the PV module or PV cell. The amount of current that a healthy cell can produce is directly proportional to its unshaded area [30,33]. In case of a cracked cell in which the crack produces an electrical disconnection of a specific area from the rest of the cell, the current of the cell will be reduced proportionally to the disconnected area. The shape of the I-V curve of the affected cell will be very similar to the nominal equivalent cell but decreasing the current proportionally to the disconnected area. The Voc is also slightly decreased. This fact can be seen in Fig. 13 to Fig. 14, cell F1. The breakage in the cell electrically disconnect some part of it (one sixth. approximately). Therefore, the Isc current in this cell will be decreased in that same proportion, from 9 A in the reference cell (F4) to 7.5 A, as seen in the I-V curve. Similarly occurs in E2, E3, E6, F6, F8 and F9.

3.3.2. EL, visual and indoor IRT characterization

The EL images of defective cells, complemented in this case by their corresponding RGB images that allow seeing the breaking patterns, are shown in Fig. 15.

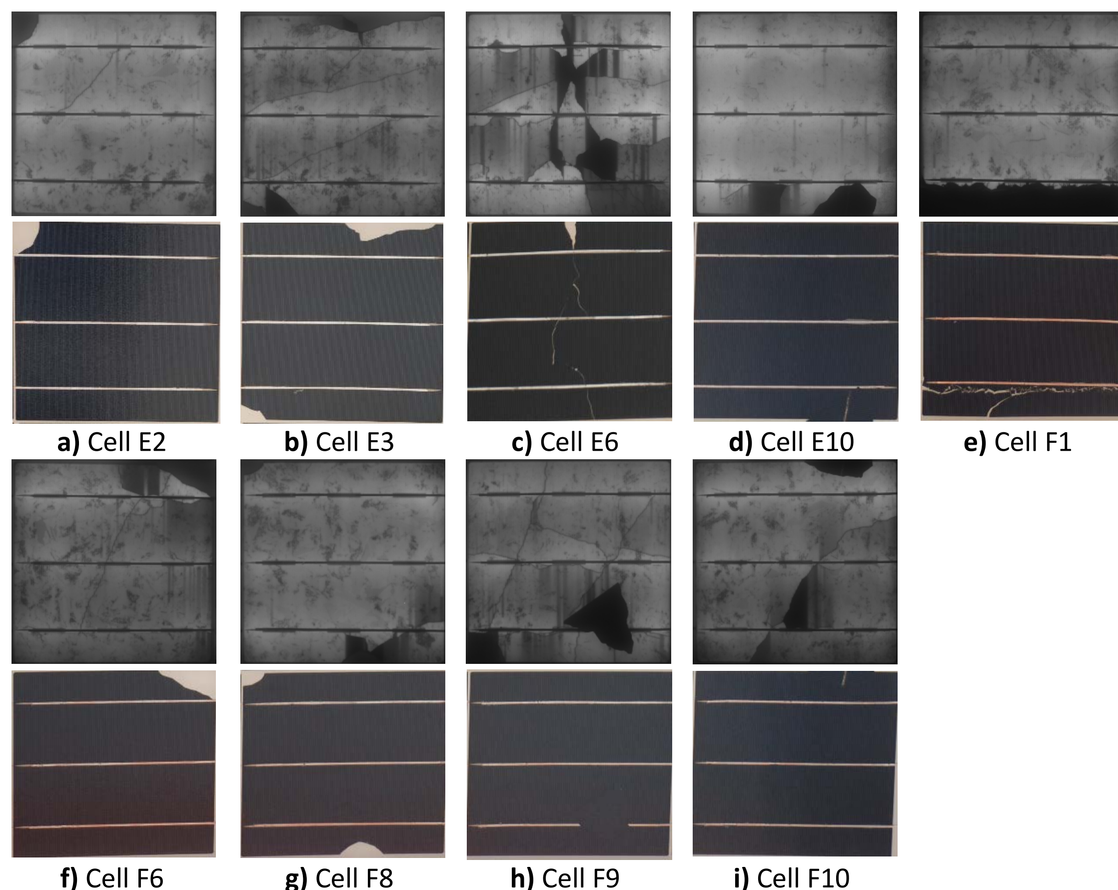

Fig. 15. EL and RGB images of the broken defective cells of the third string (string EF) with an injected current of 8.9A. EL images taken with PCO 1300 camera, with a focal distance of 4 cm and exposure time 40s.

As it can be clearly seen in Fig. 15 e), the breakage in F1 cell electrically disconnect some part of it, which corresponds with the one sixth previously cited. It is important to notice that not all

dark regions in EL corresponds with disconnected cell areas. Different is the case of cell E10, in which there is a piece of other cell over placed in the front part of the cell and it generates a parallel electrical path which is responsible of a small Rsh in the cell turning the I-V curve into a straight line, as seen in Fig. 13 cell E10.

Failures like cell cracks, solder corrosion or broken cell interconnects have no limits in power loss and the PV module may become unusable [18]. Two distinct types of dark areas are observable in the EL images (Fig. 15), irregularly shaped regions and regular rectangular shaped areas. The irregular areas indicate the presence of cracks in the silicon wafers. However, the presence of regular rectangular dark areas can be due to broken front grid fingers. which are broken at the busbar [34,35] Finally, an optical microscope has been used for imaging a crack in cell F9 solar cell, which displayed a dark irregular area in the crack zone in the EL measurement (Fig. 16). It proves how a small crack, not visible for the human eye, can isolate a part of the cell.

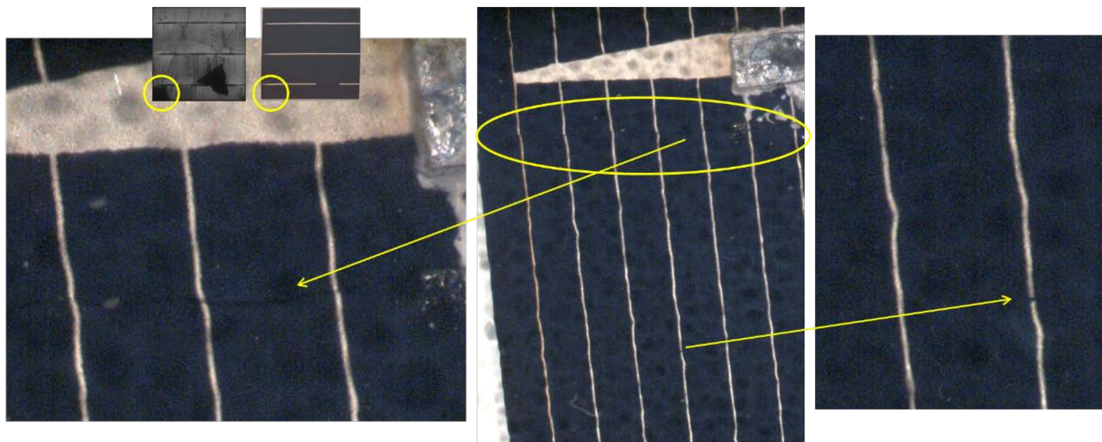

Fig. 16. Optical micrographs of a crack in F9 solar cell which displayed a dark irregular area in the crack zone in the EL. Images captured with a Nikon SMZ 800 microscope.

3.4. Defects combination /mix

When the cells are series connected, the cell which delivers the lowest current will limit the current of the string. This means that defects on a cell will determine the performance of the whole circuit. The negative impact is partly minimized by connecting bypass diodes parallel to a number of cells. Bypass diodes protect the defective solar cell from high reverse current before its breakdown voltage is reached. In typical crystalline silicon PV modules, every module string is protected by a bypass diode, although some research propose to increase the number of bypass diodes per module, up to having one per cell [36]. The maximum number of cells supported / protected by a diode is given by the cell's zener voltage.

3.4.1. I-V characterization

In this module, there is a total of three bypass diodes, one each 20 cells. As it has been seen, each bypass string contains different defects (of manufacturing, soldering and breaking cells) and each of them is able to produce a different current. Therefore, the electrical characteristic curve of the whole module, which is composed by the three bypass circuits in series, will contain three steps, each at the Isc of each bypass circuit. The electrical characteristic curves of the three bypass strings and of the module at 1,000 and 100 W/m^2 are presented in Fig. 17 and Fig. 18,

respectively. In Fig. 17, it can be seen that the most restrictive string is the breaking defects string (EF) with an Isc of 7.65A, followed by the manufacturing defects string (AB), with 8.43A and the highest current and power is in the soldering defects string, with 8.84A.

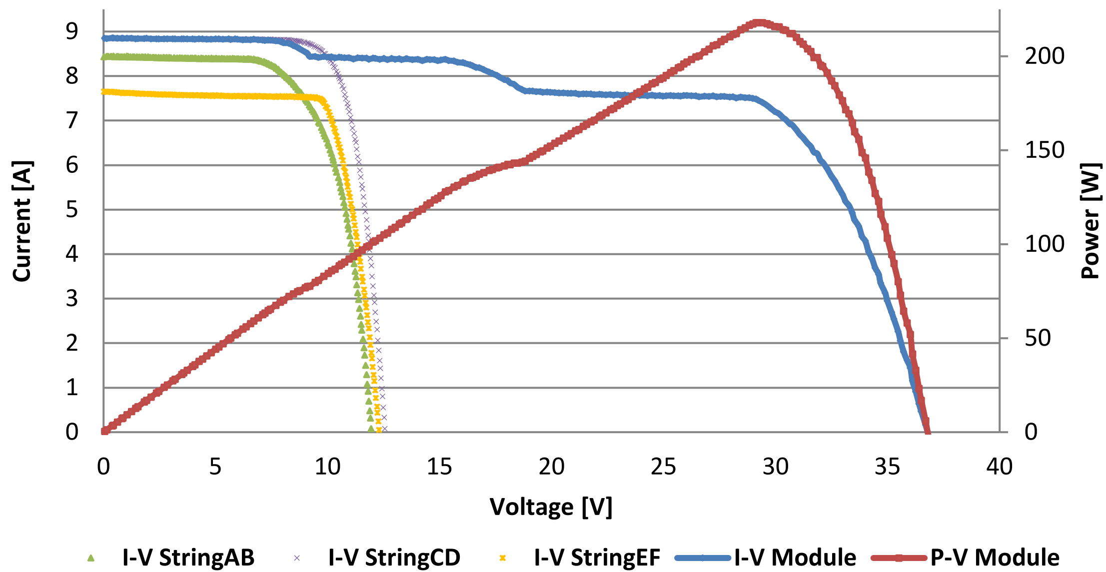

Fig. 17. I-V Curves of the complete module and separate strings at 1,000W/m^2. The secondary axis presents the P-V curves of the module at this irradiance.

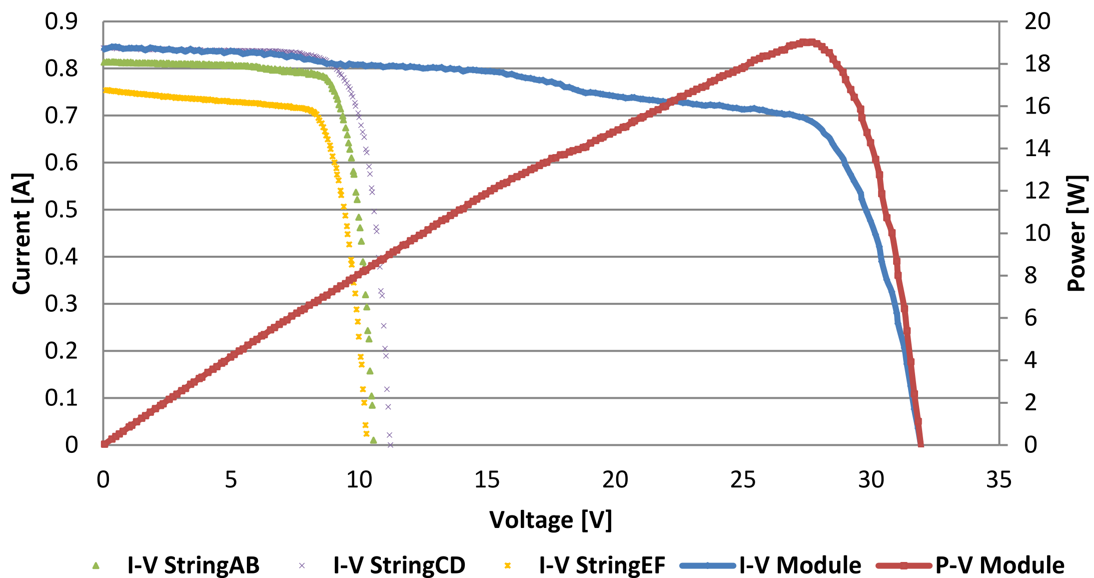

Fig. 18. I-V Curves of the complete module and separate strings at 100W/m^2. The secondary axis presents the P-V curves of the module at this irradiance.

The values of the main parameters of the I-V curve of the 3 strings measured directly in the module junction box at 1,000 W/m2 are presented in Table 6. Comparing this table with the parameters of the sum of the cells measured individually (Table 2, Table 4 and Table 5), it can be seen that the current, voltage and power values are similar or slightly lower in case of measuring the complete string in the junction box compared to the individual measurements in the case of the current or to sum of the individual measurements for the voltage and power.

This is due to the increment of resistance and the mismatch when assessing the series of cells. However, it is remarkable the soldering defects case (Table 4), which present higher Vmpp values and consequently higher power values while measuring the string. For the individual cell measurements, two buses out of the three of the cell have been taken. However, for the string measurement in the junction box, the three buses are internally connected. Therefore, it can be concluded that for soldering defects, in which the Rs has an important influence, having more buses connecting the cells could increase the module performance. Other relevant information obtained from Table 6 is the fact that although the lower Isc is obtained in the string EF (with approximately 1 A less than the others), the power generated is not the worst. In fact, the worst string is the one with the highest value of the coefficient of variation of Impp, string AB.

Table 6.
Main I-V curve parameters of the 3 strings and of the whole module measured directly in the module junction at an irradiation level of 1,000W/m^2.

String	P [W]	Impp [A]	Vmpp [V]	Isc [A]	Voc [V]
AB	67.59	7.31	9.25	8.44	11.98
CD	84.77	8.29	10.23	8.84	12.58
EF	72.91	7.39	9.87	7.64	12.32
Module	217.99	7.48	29.12	8.85	36.78

3.4.2. EL and indoor IRT characterization

The effect of a shunt resistance is particularly severe at low light levels, since there will be less light-generated current. There is a clear tendency to increase the shunt resistance on lower irradiance levels in illumination tests [37]. This effect is observable also at low injected currents while performing EL test, as seen in Fig. 19 a) and b). Following with the discussion introduced in section 3.3, this effect is extremely evident in cell E10, in which the shunt resistance increment at low injected current is responsible of appearing almost black in this case. In Fig. 14 it has been seen the impact of this high Rsh at low irradiance levels in the I-V curve. Fig. 19 c) and d) presents the indoor IRT images during this EL test. In these IRT images, it can be seen that the temperature of the manufacturing defects (cells A2 and A5) significantly increases with the injected current, being the maximum temperature of cell A2 44.6ºC and 28.5ºC with 8.9A and 0.89A injected, respectively. The rest of defects (soldering and breaking cells) experiment negligible temperature gradients compared to manufacturing defects.

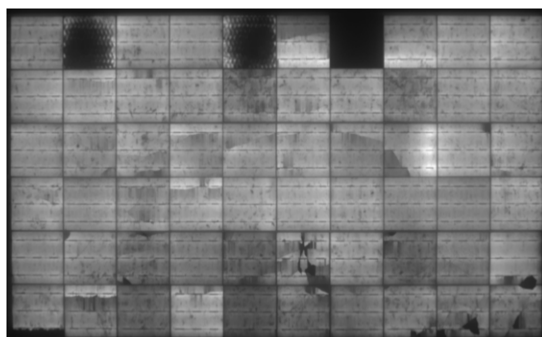
a)

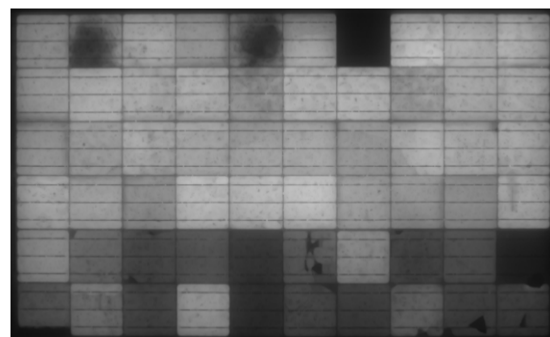
b)

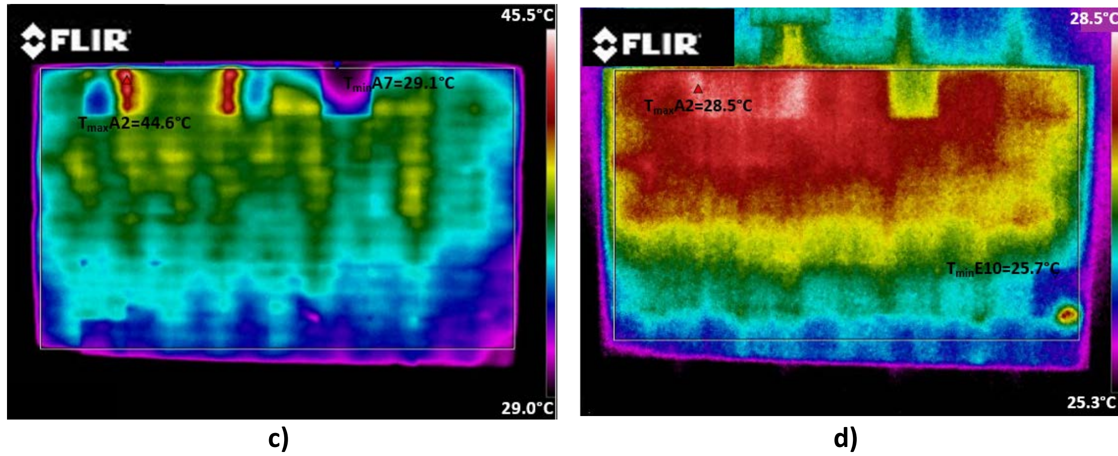

c) d)

Fig. 19. EL (a and b) and indoor IRT (c and d) images of the tested module with an injected current of 8.9A (a and c) and 0.89A (b and d). EL images taken with PCO 1300 camera, with a focal distance of 4cm and exposure time 50 s (a) and 15 min (b).

3.4.3. Outdoor IRT characterization

Two different operation points of the outdoor IRT at the irradiance of 933 W/m^2 are presented in Fig. 20, in the lower current step of the I-V curve at 7.3 A-24 V (a) and in the middle current step of the I-V curve at 7.8 A-15 V (b). These IRT images have been taken with a FLIR SC 640 IR camera. The maximum temperature values of the different hot spots are indicated in the figures. Emissivity and reflected temperature values, calculated experimentally are 0.8 and -3.5°C, respectively. In Table 7 the maximum temperatures of the main thermal defects presented in Fig. 20 and delta temperature between them and a module healthy area are presented. It is interesting to notice that delta temperature remains almost equal in A2, A5 and A7 from the first to the second operation point (from 7.3 A to 7.8 A). At the low current step, the diodes are not operating, as seen in the combiner box in Fig. 21, in which all diodes are at the same temperature (42.1°C). However, in the second current step, at 7.8 A, the temperature in F1 increases a lot, as string EF has the most restrictive current in the module and throughout the bypass diode of this string has to circulate the current that the string is not able to do.

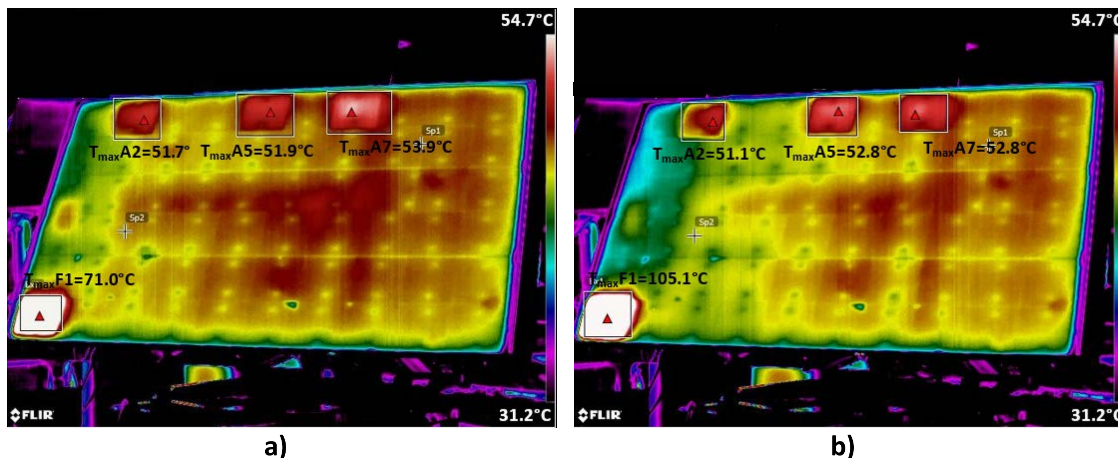

a) b)

Fig. 20. Outdoor IRT images of the module in the lower current step of the I-V curve at 7.3 A-24 V (a) and in the middle current step of the I-V curve at 7.8 A-15 V (b) at 933 W/m^2.

Table 7.
Maximum temperature of the main thermal defects presented in Fig. 20 and delta temperature between them and a module healthy area.

Operation point	7.3A and 24V (Fig. 20 a) Healthy area temperature= 47.4°C		7.8A and 15V (Fig. 20 b) Healthy area temperature= 46.6°C	
Cell	**T_{max} [°C]**	**ΔT [°C]**	**T_{max} [°C]**	**ΔT [°C]**
A2	51.7	4.3	51.1	4.5
A5	51.9	4.5	52.8	6.2
A7	53.9	6.5	52.8	6.2
F1	71.0	23.6	105.1	58.5

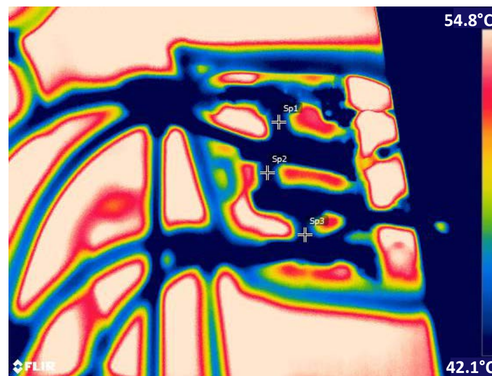

Fig. 21. Outdoor IRT images of the junction box of the module in the lower current step of the I-V curve at 7.3A and 24V. String diodes are at 42.1°C.

As it has been seen, the negative impact of faulty cells within a string is partly minimized by connecting bypass diodes parallel to a number of cells. The diode will conduct the current around the defective cell. It can be seen that in F1 hot spot heating occurs, as the rest of series connected cells (19 cells in this case) cause a reverse bias across the defective cell, that leads into a dissipation of power in this poor cell which has an area reduction of a sixth part.

In the short-circuited cell (cell A7), all the external energy received from the sun, is not used to generate electricity. The absorbed photons generate pairs of electrons in the cell material, that are recombined by other mechanisms not useful for the electricity generation and therefore, the material becomes hotter. In cell E10, although the piece of cell that has on it does not generate electricity as its upper face is not connected with nothing and it is not able to draw its energy, it also heats up, as it can be seen in Fig. 20.

3.5. Inspections concluding remark and tests validy

This section presents the concluding remark on each inspection method and defect type, to highlight the information provided by each surveying technique considering the defect type, with the aim of not missing any information during the examination. The remarks presented in this section will determine the validity of the different alternatives and their complementarity.

3.5.1. Manufacturing defects

- I-V characterization: low-efficiency and medium-efficiency defects are clearly evidenced at STC conditions, as well as the short-circuited cells. Their FF is reduced while increased

the irradiance levels and therefore their maximum power output. The efficiency defects present high values of Rs, which is shown as an increment in the curve slope at Voc. Severe defects are also revealed with a slope increment at Isc because of their reduced Rsh. Power loss can almost achieve 50% in low efficiency cells, as seen in the research.

- EL and indoor IRT characterization: low efficiency cells can be seen as a tire imprint in the EL images and they experiment a local overheating in the emitting area. Medium efficiency cells do not present any special pattern in EL neither indoor IRT, although it has been observed a tendency to decrease the light emission during EL tests with the efficiency drop. Short-circuited cells do not emit any light during EL and its whole area is seen colder in thermography, which has been denominated as *cold spot*.
- Outdoor IRT characterization: low efficiency cells as well as short-circuited cells are revealed as minor hot spots in normal outdoor operation, with a ΔT of around 5°C. Medium efficiency defects are not evidenced in outdoor IRT examination.

Therefore, the most complete inspection technique for efficiency defects is the I-V characterization. In low efficiency cells, EL complements the I-V curves with EL defects patters. Regarding the outdoor IRT, it should be very exhaustive in order to be valid, as these defects present low ΔT. In relation with short-circuited cells, EL and indoor IRT would be the most effective inspections.

3.5.2. Soldering defects

- I-V characterization: local soldering defects, in just a part of the bus, considerably increase the Rs, presenting an I-V curve affected near the Voc, incrementing the curve slope. Additionally, having one, two or all the three tabs not welded reduces the Voc.
- EL and indoor IRT characterization: soldering defects analyzed are not visible in EL. Only local soldering defects experiment an overheating during current injection. Therefore, defects with one or more buses not welded in the backside of the cell are apparently neither detectable using indoor IRT.
- Outdoor IRT characterization: soldering defects analyzed are not detectable in outdoor IRT.

It has been seen that soldering defects performed in the backside of the module present small parameter deviations than the rest of failures studied, being the I-V characterization the most effective to detect them, which can be complemented with indoor IRT in case of local soldering defects.

3.5.3. Broken cells defects

- I-V characterization: the shape of the I-V curve of the affected cell is very similar to the nominal equivalent cell but decreasing the current proportionally to the disconnected area. The Voc is also slightly decreased. Parallel electrical paths distort the I-V curve, turning it into a straight line due to small Rsh.
- EL, visual and indoor IRT characterization: EL clearly evidences disconnected areas and breaks with dark regions. Irregular areas indicate the presence of cracks in the silicon wafers while regular rectangular dark areas can be due to broken front grid fingers. Not the totality of dark regions in EL corresponds with disconnected cell areas, as the case

in which a piece of other cell is over placed in the front part of another cell. Broken cells defects analyzed have not been detected in indoor IRT.

- Outdoor IRT characterization: Disconnected areas restring the current through the cell, and this can generate a hot spot, which can reach high temperatures. The hotspot temperature will depend on the disconnected area. In the broken cell analyzed (F1), the ΔT is 23.6°C in normal operation.

Therefore, in the case of breaks in cells, the most interesting information is probably provided by the EL tests, clearly showing the breaks and disconnected areas, while outdoor IRT can complement EL locating the most restrictive cell within a string. The high resolution of the EL images enables resolving some defects more precisely than in IRT images. It has been seen in the hot spot examined that it present high ΔT, so regarding the outdoor IRT, it should not be such exhaustive as in other defects analyzed in order to be valid.

4. Conclusions and future work

Quantitative analysis and characterization of manufacturing, soldering and breaking PV defects is performed by a combination of EL, IRT, I-V curves and visual tests. Equivalent-circuit model characterization and microscope inspection are also performed as additional techniques when they contribute to the defects characterization.

In relation with the manufacturing defects, it has been seen that the most complete inspection technique is the I-V characterization. Authors propose a new term, *cold spot*, defining it as a cell or group of cells at abnormal low temperature in a PV system. Soldering defective cells present smaller parameter deviations than the rest of defects studied, with local soldering defects presenting the highest losses. Concerning broken cells, it has been analyzed how the shape of the I-V curves of the affected cells is very similar to the one of the nominal equivalent cell but decreasing the current proportionally, being the most interesting information provided by the EL tests.

As a future work, it is proposed the analysis of the same soldering defects performed on the front site of the cells instead of on the backside, in order to characterize them and compare the effect of the soldering defect location within the cell. It could be interesting seeing if they are detectable with EL and if the lack of this metal sheet in the front site generates heat differences in the front soldering defects, as well as comparing the power production. Additionally, as it has been seen that having all tabs loose may not interrupt the current in a new manufactured module, it would also be interesting to study its influence after some years of operation or after several thermal cycles. Finally, the defects characterization performed could feed a simulation program that estimates the module behavior depending on the defects combination/location within a module.

Acknowledgements

This work has been supported by Spanish national projects [ENE2017-89561-C4-R-3 and RTC-2017-6712-3] of the Spanish Ministry of Science. Innovation and Universities; the pre-doctoral research contract [from the budget application 180113-541A.2.01e691] of the University of Valladolid; and the mobility grant for short stays during the PhD [MOVILIDAD DOCTORANDOS

UVa 2019] of the University of Valladolid. Additionally, authors would like to extend our gratitude to Atersa S.L. for the manufacture of an ad hoc PV module with different defects.

References

[1] REN21. REN21 - 2019 Global Status Report. 2019.

[2] Sampaio PGV, González MOA. Photovoltaic solar energy: Conceptual framework. Renew Sustain Energy Rev 2017;74:590–601. https://doi.org/10.1016/j.rser.2017.02.081.

[3] Hernández-Callejo L, Gallardo-Saavedra S, Alonso-Gómez V. A review of photovoltaic systems: Design, operation and maintenance. Sol Energy 2019;188:426–40. https://doi.org/10.1016/j.solener.2019.06.017.

[4] Rohatgi A, Weber ER, Kimerling LC. Opportunities in silicon photovoltaics and defect control in photovoltaic materials. J Electron Mater 1993;22:65–72. https://doi.org/10.1007/BF02665725.

[5] Gallardo-Saavedra S, Hernández-Callejo L, Duque-Pérez O. Quantitative failure rates and modes analysis in photovoltaic plants. Energy 2019;183:825–36. https://doi.org/10.1016/j.energy.2019.06.185.

[6] Tsanakas JA, Ha L, Buerhop C. Faults and infrared thermographic diagnosis in operating c-Si photovoltaic modules: A review of research and future challenges. Renew Sustain Energy Rev 2016;62:695–709. https://doi.org/10.1016/j.rser.2016.04.079.

[7] Schneller EJ, Brooker RP, Shiradkar NS, Rodgers MP, Dhere NG, Davis KO, et al. Manufacturing metrology for c-Si module reliability and durability Part III: Module manufacturing. Renew Sustain Energy Rev 2016;59:992–1016. https://doi.org/10.1016/J.RSER.2015.12.215.

[8] Boix PP, Garcia-Belmonte G, Muñecas U, Neophytou M, Waldauf C, Pacios R. Determination of gap defect states in organic bulk heterojunction solar cells from capacitance measurements. Appl Phys Lett 2009;95:233302. https://doi.org/10.1063/1.3270105.

[9] Chen S, Gong XG, Walsh A, Wei SH. Defect physics of the kesterite thin-film solar cell absorber Cu 2 ZnSnS4. Appl Phys Lett 2010;96:021902. https://doi.org/10.1063/1.3275796.

[10] Gallardo-Saavedra S, Hernández-Callejo L, Duque-Perez O. Analysis and characterization of PV module defects by thermographic inspection. Rev Fac Ing Univ Antioquia 2019:92–104. https://doi.org/10.17533/udea.redin.20190517.

[11] Soultanis NL, Papathanasiou SA, Hatziargyriou ND. A Stability Algorithm for the Dynamic Analysis of Inverter Dominated Unbalanced LV Microgrids. IEEE Trans Power Syst 2007;22:294–304. https://doi.org/10.1109/TPWRS.2006.887961.

[12] Ji D, Zhang C, Lv M, Ma Y, Guan N. Photovoltaic Array Fault Detection by Automatic Reconfiguration. Energies 2017;10:699. https://doi.org/10.3390/en10050699.

[13] Silvestre S, Silva MAD, Chouder A, Guasch D, Karatepe E. New procedure for fault detection in grid connected PV systems based on the evaluation of current and voltage indicators. Energy Convers Manag 2014;86:241–9.

https://doi.org/10.1016/j.enconman.2014.05.008.

[14] Chine W, Mellit A, Pavan AM, Kalogirou SA. Fault detection method for grid-connected photovoltaic plants. Renew Energy 2014;66:99–110. https://doi.org/10.1016/j.renene.2013.11.073.

[15] Waqar Akram M, Li G, Jin Y, Chen X, Zhu C, Zhao X, et al. Improved outdoor thermography and processing of infrared images for defect detection in PV modules. Sol Energy 2019;190:549–60. https://doi.org/10.1016/j.solener.2019.08.061.

[16] Nasr Esfahani S, Asghari S, Rashid-Nadimi S. A numerical model for soldering process in silicon solar cells. Sol Energy 2017;148:49–56. https://doi.org/10.1016/j.solener.2017.03.065.

[17] Li G, Akram MW, Jin Y, Chen X, Zhu C, Ahmad A, et al. Thermo-mechanical behavior assessment of smart wire connected and busbarPV modules during production, transportation, and subsequent field loading stages. Energy 2019;168:931–45. https://doi.org/10.1016/j.energy.2018.12.002.

[18] Köntges M, Kurtz S, Packard C, Jahn U, Berger KA, Kato K, et al. Review on Failures of Photovoltaic Modules, Report IEA-PVPS T13-01:2013. 2013.

[19] Dueñas S, Pérez E, Castán H, García H, Bailón L. The role of defects in solar cells: Control and detection defects in solar cells. 2013 Spanish Conf. Electron Devices, Valladolid, Spain: 2013. https://doi.org/10.1109/CDE.2013.6481402.

[20] Fernández EF, Montes-Romero J, de la Casa J, Rodrigo P, Almonacid F. Comparative study of methods for the extraction of concentrator photovoltaic module parameters. Sol Energy 2016;137:413–23. https://doi.org/10.1016/j.solener.2016.08.046.

[21] Deviations IT. Solar I-V Curves Interpreting I-V 2014.

[22] Du B, Yang R, He Y, Wang F, Huang S. Nondestructive inspection, testing and evaluation for Si-based, thin film and multi-junction solar cells: An overview. Renew Sustain Energy Rev 2017;78:1117–51. https://doi.org/10.1016/j.rser.2017.05.017.

[23] Hallam B, Hamer P, Kim M, Nampalli N, Gorman N, Chen D, et al. Field Inspection of PV Modules: Quantitative Determination of Performance Loss due to Cell Cracks using EL Images. 2017 IEEE 44th Photovolt. Spec. Conf. PVSC 2017, 2017, p. 1858–62. https://doi.org/10.1109/PVSC.2017.8366560.

[24] Jahn U, Herz M, Köntges M, Parlevliet D, Paggi M, Tsanakas I, et al. Review on Infrared and Electroluminescence Imaging for PV Field Applications. 2018.

[25] Deitsch S, Christlein V, Berger S, Buerhop-Lutz C, Maier A, Gallwitz F, et al. Automatic classification of defective photovoltaic module cells in electroluminescence images. Sol Energy 2019;185:455–68. https://doi.org/10.1016/j.solener.2019.02.067.

[26] IEC 62446:2009 Grid connected photovoltaic systems -Minimum requirements for system documentation, commissioning tests and inspection. 2009.

[27] Buerhop C, Schlegel D, Vodermayer C, Nieß M. Quality control of PV-modules in the field using infrared-thermography. 26th Eur. Photovolt. Sol. Energy Conf. Exhib., Hamburg, Germany: n.d., p. 3894 – 3897.

[28] Suckow S. 2/3-Diode Fit 2014.

[29] National Institutes of Health. ImageJ Image Processing and analysis in Java n.d. https://imagej.nih.gov/ij/.

[30] Gallardo-Saavedra S, Karlsson B. Simulation, validation and analysis of shading effects on a PV system. Sol Energy 2018;170:828–39. https://doi.org/10.1016/j.solener.2018.06.035.

[31] Herrmann W, Wiesner W, Vaassen W. Hot spot investigations on PV modules - new concepts for a test standard and consequences for module design with respect to bypass diodes. Conf Rec IEEE Photovolt Spec Conf 1997:1129–32. https://doi.org/10.1109/pvsc.1997.654287.

[32] Honsberg C, Bowden S. Photovoltaics Education Website 2019. www.pveducation.org.

[33] Rezk H, AL-Oran M, Gomaa MR, Tolba MA, Fathy A, Abdelkareem MA, et al. A novel statistical performance evaluation of most modern optimization-based global MPPT techniques for partially shaded PV system. Renew Sustain Energy Rev 2019;115:109372. https://doi.org/10.1016/j.rser.2019.109372.

[34] Chaturvedi P, Hoex B, Walsh TM. Broken metal fingers in silicon wafer solar cells and PV modules. Sol Energy Mater Sol Cells 2013;108:78–81. https://doi.org/10.1016/j.solmat.2012.09.013.

[35] Munoz MA, Alonso-García MC, Vela N, Chenlo F. Early degradation of silicon PV modules and guaranty conditions. Sol Energy 2011;85:2264–74. https://doi.org/10.1016/j.solener.2011.06.011.

[36] Hanifi H, Pander M, Jaeckel B, Schneider J, Bakhtiari A, Maier W. A novel electrical approach to protect PV modules under various partial shading situations. Sol Energy 2019;193:814–9. https://doi.org/10.1016/j.solener.2019.10.035.

[37] Ruschel CS, Gasparin FP, Costa ER, Krenzinger A. Assessment of PV modules shunt resistance dependence on solar irradiance. Sol Energy 2016;133:35–43. https://doi.org/10.1016/j.solener.2016.03.047.